

X-ray Characterization of a Multiferroic Bismuth Ferrite Thin Film

Undergraduate Researcher

Brian Mikolajczyk
Northwestern University

Faculty Mentor

Michael Bedzyk
Department of Materials Science and Engineering
Northwestern University

Graduate Student Mentors

Jeffrey Klug
Department of Physics and Astronomy
Northwestern University

Jui-Ching Lin

Department of Materials Science and Engineering
Northwestern University

Abstract

Numerous studies have been structured to investigate magnetoelectric multiferroic materials, which possess simultaneous ferroelectric and (anti)ferromagnetic ordering. Bismuth ferrite (BiFeO_3), referred to as BFO, has drawn special attention because of its unique ability to maintain both electric and magnetic dipole moments at room temperature. BFO shows great potential to revolutionize the microelectronics industry, but there are impediments to its application in devices. This study was designed to use high-resolution x-ray diffraction (HRXRD) and low-angle x-ray reflectivity (XRR) techniques to investigate the single-crystal quality of a BFO thin film. The BFO thin film was grown by pulsed-laser deposition (PLD) on a strontium ruthenate (SrRuO_3) (referred to as SRO) intermediate layer, which was grown atop an (001)-oriented strontium titanate (SrTiO_3 referred to as STO) substrate. X-ray characterization techniques found the BFO film to experience contraction strain in the transverse direction and extension strain in the axial direction; therefore, it was concluded that the BFO thin film was, relatively speaking, coherently strained. Additionally, the film showed a minute mosaic, indicating it was a high-quality thin film with good single-crystal attributes. Further studies are needed to demonstrate the effectiveness of the SRO layer on the single-crystal growth of the BFO thin film. Future research should also include a systematic study comparing the growth of BFO thin films across different growth techniques.

Introduction

Interest in multiferroic materials, which show simultaneous ferroelectric and magnetic order parameters, has greatly increased in the past few years.¹ From an applications perspective, the magnetoelectric coupling between magnetic and ferroelectric phenomena in one material could lead to a new generation of multifunctional devices, where magnetism is controlled by voltages, instead of by magnetic fields. Coupling could permit data to be written electrically and read magnetically, thus exploiting the best aspects of ferroelectric random access memory (FeRAM) and magnetic data storage, while avoiding the problems linked to reading FeRAM and generating the large local magnetic fields needed to write.^{2,3} Multiferroic thin films can be employed in the manufacture of a plethora of microelectronic devices, including microactuators, nonvolatile ferroelectric random-access memories (NVRAM), infrared sensors, thermal infrared switches, and dynamic random-access memory (DRAM) storage capacitors.⁴

Bismuth ferrite (BiFeO_3), commonly referred to as BFO, is a material that lately has drawn attention because of its multiferroic properties at room temperature, specifically the coexistence of both ferroelectric and antiferromagnetic ordering.^{1,5} Unfortunately, even the thinnest single-crystal BFO films show high coercive fields and high leakage currents, which present an obstacle to device applications.⁴ Studying the film morphology, interface structure, in-plane crystallinity, and other single-crystal qualities of BFO films can result in better understanding of these impediments to BFO device applications. High-angle XRR techniques make it possible to analyze the multiferroic thin films and

X-ray Characterization of a Multiferroic Bismuth Ferrite Thin Film *(continued)*

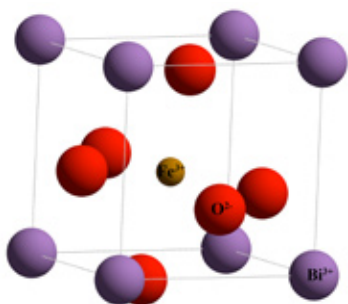


Figure 1. Crystal structure of a BFO perovskite pseudo-cubic unit cell. There is a slight displacement along the (111) body diagonal direction between the anion (O^{2-}) sublattice and the cation (Fe^{3+} and Bi^{3+}) sublattices. This produces an electric dipole moment along the (111) direction.

correlate the structural properties to the epitaxial growth processes, the electrical and magnetic properties, and the device performance.^{6,7} In this experimental study high-resolution x-ray diffraction (HRXRD) and XRR were performed to study the single-crystal quality of a BFO thin film. The BFO film was grown on a SRO layer, which was in turn grown on an STO. Due to lattice parameter mismatch, the BFO thin film grown on an STO substrate should experience contraction strain in the in-plane direction and extension strain in the out-of-plane direction. Diffraction data were used to analyze thicknesses, miscut, out-of-plane lattice constants, in-plane lattice constants, mosaic, and strain due to lattice mismatch. At the same time, reflectivity data were fit to theory to calculate the interface structure and film morphology, specifically thickness and interface roughness.

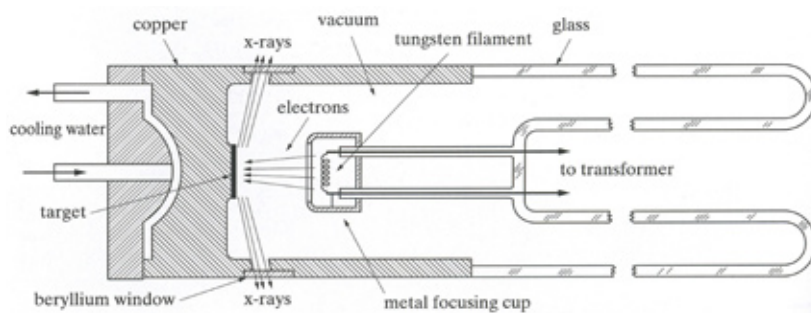


Figure 2. Cross-sectional diagram of a sealed x-ray tube.¹²

Background

BFO is an oxide belonging to the perovskite family, whose compounds have the general formula ABO_3 , where A is a monovalent, divalent, or trivalent metal, and B is a pentavalent, tetravalent, or trivalent element, respectively; for BFO, both bismuth and iron are trivalent to balance the negative six charge of the three oxygen atoms.⁸ BFO is a magneto-electric multiferroic material that simultaneously possesses ferroelectric and antiferromagnetic properties that can be coupled. Ferroelectric crystals possess cooperative ionic displacements that cause a stable and switchable electrical polarization, whereas ferromagnetic crystals possess a stable and switchable magnetization due to exchange, which is a quantum mechanical occurrence.³ In bulk, the crystal structure of a BFO unit cell is hexagonal rhombohedral. The center of the oxygen anions' unit cell is slightly displaced from the center of the unit cells for each of the two cations (Figure 1). This separation of charge

creates a net electric dipole moment, which gives the compound its ferroelectric properties.⁸ The magnetic structure of BFO was a mystery for many years, as some laboratories claimed it to be antiferromagnetic, while others claimed it to be weakly ferromagnetic.⁹ BFO has long been known to be an antiferromagnetic ferroelectric multiferroic in bulk form. Antiferromagnets are materials with ordered magnetic dipole moments that cancel each other out completely within each unit cell of the crystal. The magnetic dipoles originate from the unpaired spins on the Fe^{3+} cations. However, it was recently discovered that there might be a slight canting of the antiferromagnetic sublattices of BFO, which would result in a net macroscopic magnetization, referred to as weak ferromagnetism.¹⁰

X-rays are a form of electromagnetic radiation with high energies and wavelengths on the scale of angstroms.¹¹ Every x-ray diffractometer setup in this

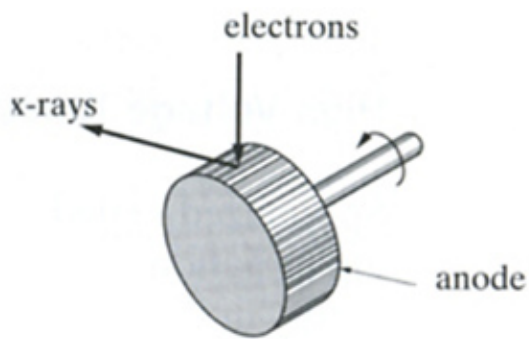


Figure 3. Illustration of a rotating-anode for an x-ray tube.¹²

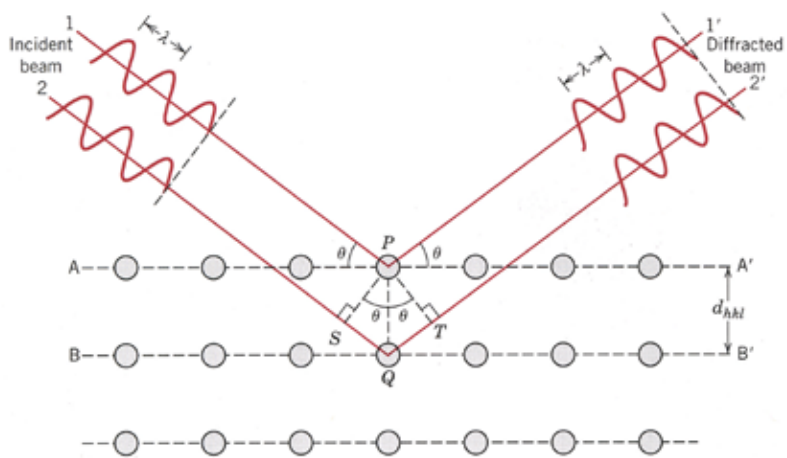


Figure 4. Schematic of diffraction of x-rays by planes of atoms.¹¹

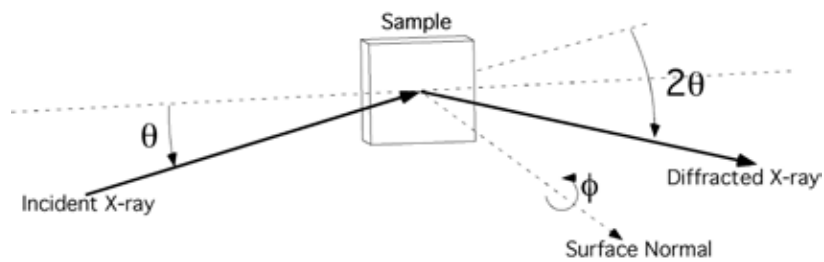


Figure 5. Illustration of an x-ray diffractometer. Incident x-rays, produced by the x-ray tube, contact the sample surface at an incident angle of θ . The x-rays reflect off the sample and are measured by a detector at an angle 2θ . The sample rotation about its own axis is measured as an angle ϕ .

X-ray Characterization of a Multiferroic Bismuth Ferrite Thin Film (continued)

work uses a Cu rotating-anode x-ray source (Figures 2 and 3). This x-ray source contains two electrodes in high vacuum: the copper anode target and the cathode filament. The anode is maintained at ground potential, whereas the cathode is maintained at a high negative potential. The cathode filament, commonly tungsten, is heated by a current, which causes the filament to emit electrons. These electrons are repulsed away by the high negative potential and accelerated toward the copper target. When the electrons collide with the copper target, they decelerate. If they possess sufficient energy, they will cause inner-shell electrons from copper atoms to be ejected. Electrons from higher energy levels within the copper atoms drop to lower energy levels in order to fill the vacancy left by the ejected electrons. The transition with the highest probability causes the copper atom to emit Cu $K\alpha_1$ x-ray fluorescence radiation with an energy of $E_\gamma = 8.048$ KeV and a corresponding wavelength of $\lambda = 1.5405$ Å. The single-crystal x-ray monochromator, which is in line between the x-ray source and the sample, uses Bragg diffraction to pass this wavelength.¹² From this point the x-rays can be utilized to determine the crystal structures of solids.

Because x-rays have wavelengths comparable to the spacings of atoms, x-ray diffraction techniques have historically been utilized to investigate the crystal structure of solids. The phenomenon of diffraction occurs when a wave comes across an obstruction that is capable of shattering the wave and has equally-spaced obstacles. Diffraction is a result of multiple waves being scattered in different ways such that the paths they traverse is different; essentially, diffraction is caused by differences in phase relationships. The diffraction of a

monochromatic, collimated x-ray beam after it encounters a periodically arranged set of atomic planes is given by Bragg's law: $n\lambda = 2d_{hkl}\sin\theta$, where n is an integer value known as the order of reflection, λ is the wavelength in angstroms, d_{hkl} is the interplanar spacing that separates the planes of atoms in angstroms, and is the incident angle in degrees. As shown in Figure 4, the path length difference (SQT) is equivalent to $2d_{hkl}\sin\theta$. If this path length difference equals an integer multiple of the wavelength, then the two waves along the two paths constructively interfere, and a Bragg diffraction peak is observed. In this simple ideal picture, if the angle θ is detuned from the Bragg condition, waves from the very large set of planes will cancel out in pairs. The magnitude of the interplanar spacing for a cubic lattice is

$$d_{hkl} = \frac{a}{\sqrt{h^2 + k^2 + l^2}}$$

where h , k , and l are the Miller indices, and a is the lattice constant.¹¹ Miller indices are coordinates in reciprocal space used to describe lattice planes and directions in a crystal; they are typically given as (hkl) .¹³

To illustrate high-angle XRR for thin films, the sample must be scanned at high angles in the vicinity of the Bragg peaks of the substrate, intermediate layer and film. If the sample orientation is (001) , for example, scanning will be executed along the $(00L)$ Bragg peaks, where L is generally a positive integer value. When scanning, the diffractometer instrumentation is constructed so that the sample rotates at an angle θ , while the detector arm moves at an angle 2θ (Figure 5). Thus, scans involving the rotation of the sample by θ and the

rotation of the detector arm by 2θ are called θ - 2θ scans. Eventually, the x-ray scattering from the sample through the $(00L)$ peaks of the substrate, intermediate layer and film will be measured along Q , a wavelength-independent wave vector that is perpendicular to the surface, as opposed to θ . The equation for Q is given

$$\text{by } Q = \frac{4\pi \sin \theta}{\lambda}. \text{ The counts}$$

measured by the detector are later converted to counts per second (cps), which, when divided by the straight-through beam intensity in cps, gives a unit-less quantity known as reflectivity. When plots are made with reflectivity on the y-axis and Q on the x-axis, there are generally two important observations to make. First, the Bragg peaks of the substrate and the film should be noticeably different. The sharpest peak is the $(00L)$ substrate peak, while a broader peak will belong to a thin film or intermediate layer; the film's broader $(00L)$ Bragg peak is attributed to its finite thickness, and the same is true of the intermediate layer. Second, the intensity of the film and the intermediate layer is spread into oscillations surrounding the Bragg peaks. Together, the Bragg peaks and surrounding oscillations, commonly referred to as thickness fringes, form the sample's specular crystal truncation rod (CTR).¹⁴ This CTR scanning, essentially specular reflectivity scans in reciprocal space along the $(00L)$ Bragg peaks, is commonly utilized to extract diffraction data, including thicknesses, lattice constants, strain and miscut.

Low-angle XRR investigations have also gathered information on thin-film structures. For electromagnetic radiation with frequencies in the x-ray region, the

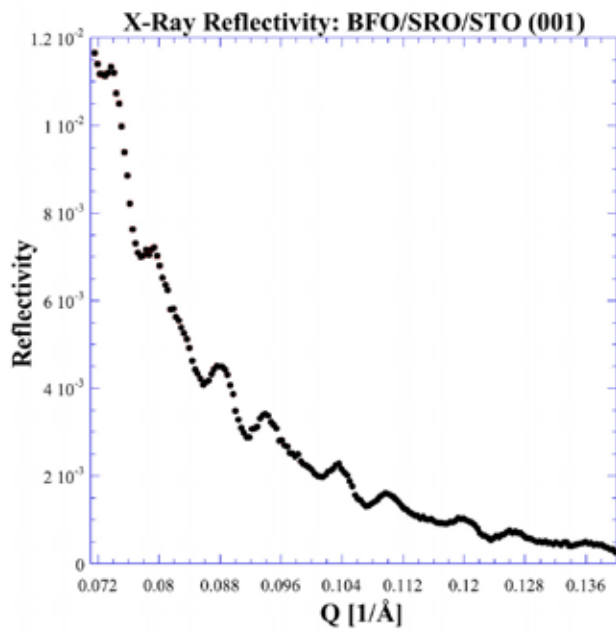


Figure 6. XRR profile with a small Q-range of $0.071\text{--}0.14 \text{\AA}^{-1}$.

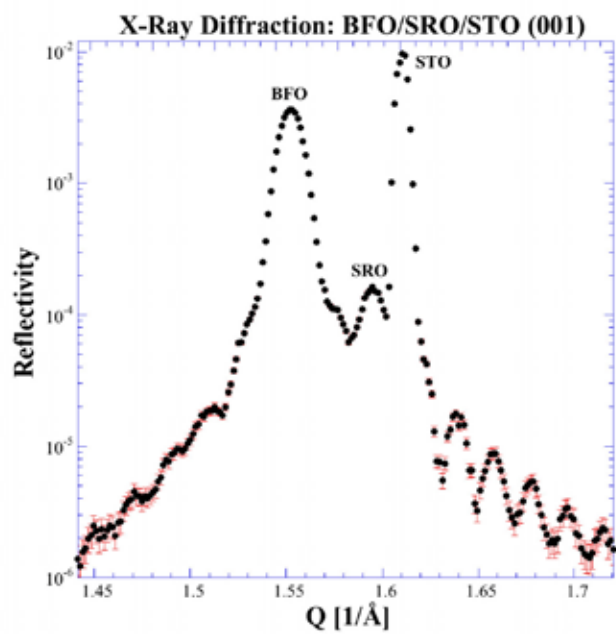


Figure 7. CTR profile around the (001) Bragg peaks with a Q-range of $1.44\text{--}1.72$.

refractive index of transparent materials, n , is less than unity. The refractive index equation is

$$n = 1 - \delta, \text{ with } \delta = \frac{2\pi\rho r_0}{k^2},$$

where δ is the deviation of n from unity, ρ is the electron density, r_0 is the Thomson scattering amplitude, and the x-ray wavelength, λ , is related to the

wavevector, k , by $k = \frac{2\pi}{\lambda}$. Because of

this, incident x-rays with glancing angles below a certain critical angle α_c will no longer penetrate into the material but will be totally reflected from it; this phenomenon is known as total external reflection. Because n is only slightly less than unity, the critical angle is miniscule and is given by $\alpha_c = \sqrt{2\delta}$, which is typically

on the scale of milliradians. As with diffraction data gathering, θ - 2θ scans are performed, but at low angles for reflectivity. Reflectivity will be at a maximum of 1, indicating total external reflection, until the critical angle, which signifies the point where reflectivity begins to drop off. During this period of decreasing reflectivity, thickness fringes are typically noticeable in the low-angle reflectivity profile. Measuring the period of these oscillations is crucial in determining film thicknesses. Reflectivity data can also be fit to Fresnel theory, which can provide information regarding interface roughness.¹⁵

Approach

The BFO film was grown on an SRO layer by pulsed-laser deposition (PLD) on an (001)-oriented STO substrate by collaborator Ying-Hao Chu in the Ramesh research group at the University of California, Berkeley. The sample dimensions were approximately 5 mm by

5 mm by 0.5 mm. To study the structure, HRXRD measurements were performed on a four-circle diffractometer with a 12 kW rotating-anode x-ray source operated at 40 KV and 100 mA and a sagittally focusing graphite monochromator crystal. The incident photon flux through the 0.5-mm-wide by 1-mm-high slit was 1.05×10^7 photons/second, and instrument resolution was 0.007 \AA^{-1} .

Low-angle XRR measurements were also performed on a Rigaku ATX-G rotating-anode four-circle diffractometer. The ATX-G is an 18 kW (maximum) machine operated at 50 KV and 240 mA. The incident beam was conditioned by a Ge (111) asymmetric channel cut and a 0.05-mm-wide by 2-mm-high incident beam slit. The incident photon flux was 2.6×10^6 photons/second. Instrument resolution was determined to be 0.002 \AA^{-1} . All x-ray experiments were conducted at the Northwestern University X-Ray Facility, using a Cu K α 1 x-ray wavelength of 1.5405 \AA . Additionally, both diffraction and reflectivity data were background subtracted and normalized to their respective straight-through beam intensities.

The x-ray diffraction specular CTR profile provides data necessary to compute thickness and out-of-plane lattice constants. The period of thickness fringes is calculated in units of \AA^{-1} as ΔQ , and the thickness of a particular

film is calculated by $t = \frac{2\pi}{\Delta Q}$. Also, the

domain size, D_{hkl} , of a film can be determined from its full-width half maximum (FWHM) by

$$D_{hkl} = \frac{5.91}{FWHM_{film}}, \text{ where the domain}$$

size equals the thickness, t , if the film is coherently strained throughout. The

out-of-plane lattice constants are calculated using Bragg's law, the equation for Q , and the equation for the magnitude of the interplanar spacing. When looking at the (001) Bragg peaks, the equation for the magnitude of the interplanar spacing indicates that the out-of-plane lattice constant is equal to the d-spacing, d_{001} . With Bragg's law and the equation for Q , algebraic manipulation provides the equation for the (001) d-spacing:

$$d_{001} = \frac{2\pi}{Q}. \text{ However, because the}$$

out-of-plane lattice constant, a , is equal

to d_{001} , it follows that $a = \frac{2\pi}{Q}$. This

means that $a_{BFO} = \frac{2\pi}{Q_{BFO}}$, $a_{SRO} = \frac{2\pi}{Q_{SRO}}$ and $a_{STO} = \frac{2\pi}{Q_{STO}}$ when looking at the

(001) CTR profile. For the (002) CTR profile, the same procedure is used for the most part, but now a is equal to twice the d-spacing, d_{002} , i.e., $a = 2d_{002}$. This

implies that $a = \frac{4\pi}{Q}$, which means that

$$a_{BFO} = \frac{4\pi}{Q_{BFO}}, a_{SRO} = \frac{4\pi}{Q_{SRO}} \text{ and}$$

$a_{STO} = \frac{4\pi}{Q_{STO}}$ when looking at the (002)

CTR profile. The film miscut, the difference between surface and crystallographic planes, is determined by performing θ scans at different values of ϕ , which involves rotating the sample about its own axis (Figure 5). The values of ϕ and θ are subsequently plotted as (ϕ , θ) pairs and fitted with a vertically and horizontally modified cosine function; the miscut value is given in degrees and is equal to the fitted amplitude of the cosine function.

To examine the in-plane crystal-quality of the film, diffraction measurements were made in the off-normal crystallographic direction of (101). The instrumentation was calibrated in the STO (101) direction such that (101) referred to the STO (101) direction. In-plane scans were conducted to find the (hkl) coordinates of the BFO Bragg peak. It is important to note that scanning was performed in the H direction as opposed to the L direction because scanning the H direction gives in-plane position, whereas scanning the L direction would give out-of-plane position. The reciprocal of the h-coordinate of the BFO peak gives the ratio of the BFO in-plane lattice constant to the STO bulk lattice constant. Thus, the BFO in-plane lattice constant can be computed by multiplying this ratio by the STO bulk lattice constant.

STO is a common substrate for epitaxial growth, which is the growth of a thin film on a substrate, creating a film-substrate interface; at room temperature and atmosphere, the crystal structure of an STO unit cell is primitive cubic with a bulk lattice constant of 3.905 Å. In bulk, SRO has an orthorhombic unit cell, and BFO has a hexagonal rhombohedral unit cell; however, both SRO and BFO have a pseudocubic structure within their respective bulk unit cells. Thus, SRO is said to be an orthorhombically distorted cubic perovskite, whereas BFO is understood to be a rhombohedrally distorted cubic perovskite. Because of its primitive cubic structure and close match in lattice constant, STO is thought to be a good substrate for SRO and BFO epitaxial growth. The SRO and BFO bulk lattice constants, 3.923 Å and 3.964 Å, respectively, are slightly larger than 3.905 Å. Therefore, they experience

transverse in-plane strain, which causes axial out-of-plane strain. The transverse strain is computed as

$$\epsilon_{\parallel} = \frac{a_{\parallel}^{film} - a_{\parallel}^{bulk}}{a_{\parallel}^{bulk}},$$

while the axial strain is computed as

$$\epsilon_{\perp} = \frac{a_{\perp}^{film} - a_{\perp}^{bulk}}{a_{\perp}^{bulk}},$$

where $a_{\parallel}^{bulk} = a_{\perp}^{bulk} = 3.964 \text{ \AA}$.¹⁶ Using

the transverse and axial strain values, Poisson's ratio can be measured. This ratio measures the tendency of materials to contract in directions transverse to the direction of extension. The value of Poisson's ratio is calculated as the negative of the transverse strain divided by the axial strain:

$$\nu = -\frac{\epsilon_{\parallel}}{\epsilon_{\perp}},$$

where the transverse and axial strains are calculated as above. Most practical materials typically have ν values between 0 and 0.5.¹⁷ Metal oxides usually have ν values around 0.25.¹⁸

The single-crystal quality of the BFO film was investigated using transverse θ scans; these scans are commonly referred to as rocking curve scans because they are executed at a fixed 2θ , while the θ angle rocks through the diffraction peak. If a film is amorphous, meaning it lacks form and is therefore noncrystalline, it would lack a periodic arrangement of atoms. Due to these conditions, diffraction cannot be observed for amorphous materials. If a film is a polycrystalline, it essentially is a large collection of randomly oriented single-crystal grains. Polycrystalline samples will produce

Bragg peaks without surrounding thickness fringes in the CTR profile, but there will in fact be more Bragg peaks than expected, since scanning along any random direction for a polycrystalline sample is effectively scanning every direction. More important, θ rocking curve scans maintain a constant value without producing a peak. This is because of scattering from all the grains, which have no preferred orientation. However, if diffraction peaks from the film are observed at a given 2θ and a small range of θ , then the film is said to be single-crystal.¹¹ The width of the rocking curves gives information regarding the mosaic structure of the sample. Though a film may be single-crystal with a preferred orientation, it can still possess a mosaic structure of slightly misoriented subgrains if it has a large lattice mismatch with its substrate. The mosaic of an epitaxial film can be described by the range of angle that the subgrains have with respect to the substrate normal, which is quantitatively expressed as the FWHM of the surface normal x-ray rocking curve.¹⁹ This FWHM is commonly referred to as a parameter to assess the film quality, with smaller FWHM indicating a smaller mosaic and thus a better quality film. Other properties that also affect this FWHM are instrument resolution and in-plane domain size.

Finally, the analyzed low-angle XRR profile provides information regarding total film thickness, as well as the roughness values of the three interfaces: between STO and SRO, between SRO and BFO, and between BFO and air, which is regarded as both a surface and an interface. The thickness fringes in the reflectivity profile can be analyzed the same as the diffraction thickness fringes,

X-ray Characterization of a Multiferroic Bismuth Ferrite Thin Film (continued)

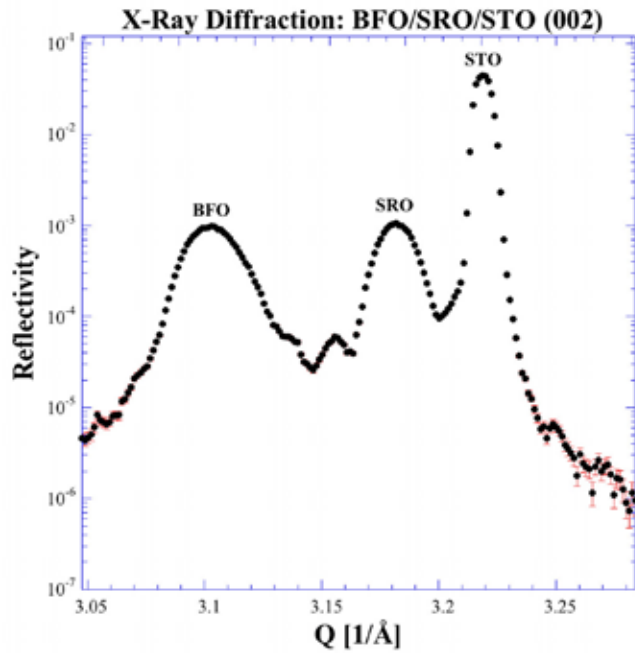


Figure 8. CTR profile around the (002) Bragg peaks with a Q-range of 3.05–3.28.

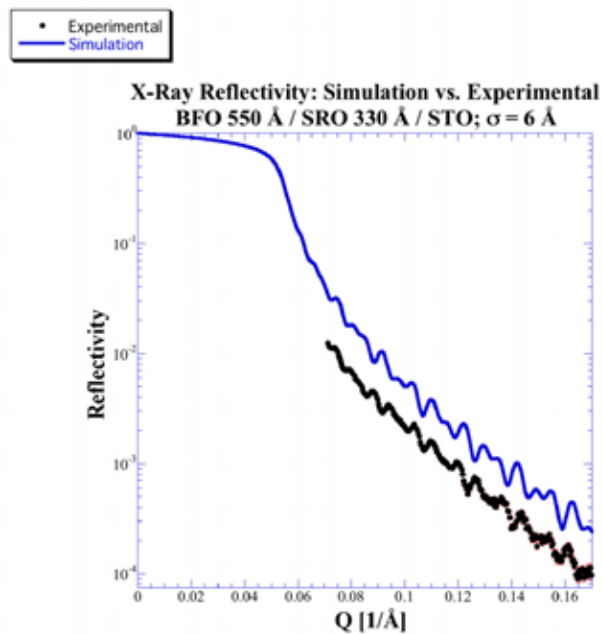


Figure 9. XRR profile comparing Fresnel theory simulation to experimental data. Simulation data are shown for a Q-range of 0–0.17 \AA^{-1} , or 0–1.19°, whereas experimental data are only shown for a Q-range of 0.071–0.17 \AA^{-1} , or 0.5–1.19°.

i.e., $t_{\text{total}} = \frac{2\pi}{\Delta Q}$. Low-angle XRR can

be simulated using Fresnel theory, and the roughness values for the three interfaces can be adjusted until the simulation appropriately fits the data.

Results and Discussion

Low-angle XRR measurements were performed up to $2\theta = 4^\circ$, and thickness fringes were analyzed to calculate the total thickness of the SRO layer and BFO film. Figure 6 displays a small portion of the reflectivity scan with good-quality thickness fringes. The period of these thickness fringes was calculated to be approximately 0.0071 \AA^{-1} . This corresponds to a total thickness of 880 \AA , indicating the thickness of the BFO thin film plus the SRO intermediate layer is 880 \AA . High-angle diffraction measurements, as well as low-angle XRR simulation, were utilized to calculate the specific thicknesses of BFO and SRO.

High-angle x-ray diffraction measurements were made around the (001) and (002) Bragg peaks of the sample. Thickness fringes were measured from the (001) CTR profile, which is shown in Figure 7. The thickness fringes above the Bragg peaks exhibited a period of 0.019 \AA^{-1} . This translates to a thickness of 330 \AA . The FWHM of the SRO Bragg peak could not be measured in the (001) CTR profile due to Bragg peak-crowding; however, the FWHM_{SRO} could be sufficiently measured in the (002) profile, which demonstrated a FWHM_{SRO} of 0.018 \AA^{-1} (Figure 8). This FWHM corresponds to an SRO out-of-plane domain size of 330 \AA . These results indicate that the thickness of the intermediate SRO layer is equal to this domain size, which equals 330 \AA . With the XRR-determined total thickness

being 880 \AA and the SRO intermediate layer thickness being 330 \AA , the BFO thin-film thickness can be approximated as the difference, which is 550 \AA . Because of this, it is apparent that the SRO thin film is coherently strained throughout, and that the CTR profile of the sample only shows thickness oscillations from the SRO intermediate layer and not the BFO thin film. This is consistent with the fact that the modulations from thicker films are typically more difficult to see in the CTR profile. The BFO film is also less coherent than the SRO film.

Low-angle XRR experimental measurements were compared with a simulation using Fresnel theory. The simulation used a fixed SRO thickness of 330 \AA and a fixed BFO thickness of 550 \AA ; this allowed the roughness parameter to be adjusted until the simulation's slope effectively fit the data's. As Figure 9 shows, this is accomplished with a roughness, σ , of 6 \AA . Simply matching the simulation with the experimental results indicates that the SRO intermediate layer thickness is 330 \AA , the BFO thin-film thickness is 550 \AA , and the roughness of the three interfaces is on the scale of 6 \AA .

The miscut was calculated using the STO (001) Bragg peak by performing θ scans at different angles of ϕ . The θ scans were executed at ϕ intervals of 45° and then plotted with the θ values on the y-axis and the ϕ values on the x-axis. As illustrated in Figure 10, a vertically and horizontally modified cosine function is fitted to the data. The generic function is

$$\theta^{\text{peak}} = \theta_{\text{average}}^{\text{peak}} + \alpha * \cos(\phi - \gamma);$$

particular values for the fit were

$$\theta_{\text{average}}^{\text{peak}} = 11.404^\circ, \alpha = 0.186^\circ, \text{ and}$$

$$\gamma = -46.433^\circ. \text{ However, it is the value of}$$

α that is most important, because that is precisely the value of the miscut; thus, the film miscut is 0.186° .

The (001) and (002) CTR profiles were investigated to find the value of Q at which the BFO Bragg peak occurred; this data were used to find the BFO out-of-plane lattice constant. The value of Q at the BFO (001) Bragg peak was 1.553 \AA^{-1} (Figure 7); this corresponds to a BFO out-of-plane lattice constant of 4.047 \AA . The value of Q at the BFO (002) Bragg peak was 3.103 \AA^{-1} (Figure 8). The value corresponds to a BFO out-of-plane lattice constant of 4.049 \AA . It is evident that the out-of-plane lattice constant calculations were consistent across the (001) and (002) Bragg peaks; additionally, the BFO out-of-plane lattice constant is clearly greater than its lattice constant in bulk (3.964 \AA).

The in-plane lattice constants were calculated by making x-ray diffraction measurements in the off-normal (101) direction. By scanning in plane, the (hkl) coordinates of the broad BFO peak were found; the h-coordinate of the peak was 0.9904 . This denotes that the ratio of the STO bulk lattice constant to the BFO in-plane lattice constant is 0.9904 ; in other words, this signifies that the BFO in-plane lattice constant is approximately 1% larger than the STO bulk lattice constant. Multiplying the STO bulk lattice constant by the reciprocal of the ratio yields the in-plane BFO lattice constant. In this experiment the in-plane BFO lattice constant was calculated as 3.943 \AA , which is clearly less than its bulk lattice constant.

The fact that the BFO bulk lattice constant is less than the experimental out-of-plane lattice constant and greater than the in-plane lattice constant is

X-ray Characterization of a Multiferroic Bismuth Ferrite Thin Film *(continued)*

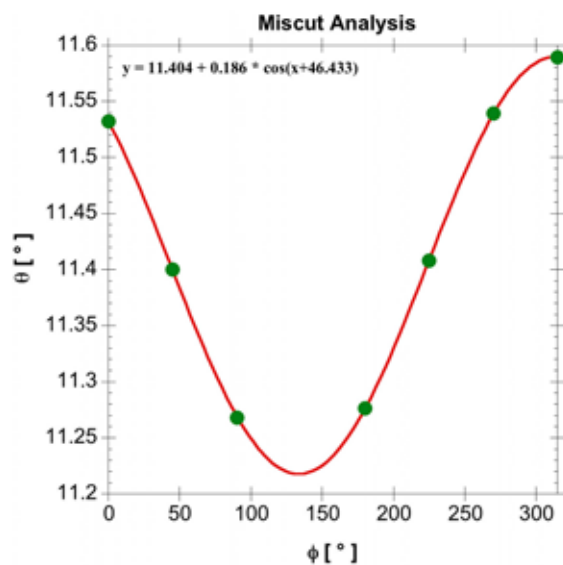


Figure 10. Miscut analysis with fit and equation shown. The graph contains ϕ values of 0°, 45°, 90°, 180°, 225°, 275°, and 315°, with corresponding θ values of 11.53°, 11.4°, 11.27°, 11.28°, 11.41°, 11.54°, and 11.59°.

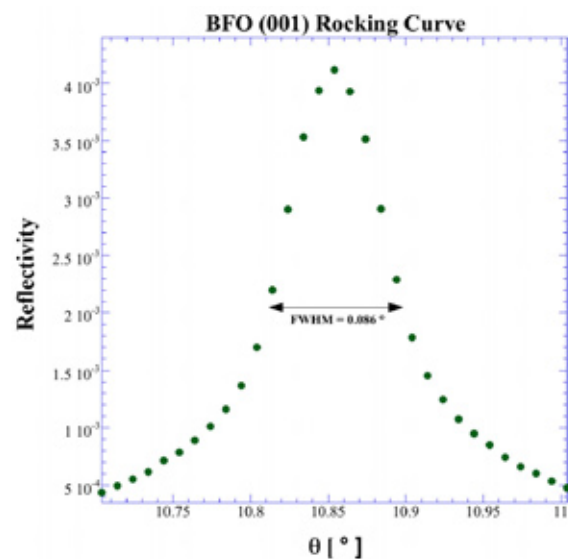


Figure 11. Rocking curve around the BFO (001) Bragg peak. Diffractometer was centered at $2\theta=21.94^\circ$ and $\theta=10.85^\circ$, and rocking curve was executed at 0.15° .

consistent with elasticity theory. The BFO thin film, as well as the SRO intermediate layer, is grown atop an (001)-oriented STO substrate; thus, both SRO and BFO pseudo-cubic lattice constants will be compressively strained to conform to the STO bulk lattice constant in the in-plane direction. This contraction strain in the in-plane direction is relieved in the out-of-plane direction, where the lattice constant is expected to be larger than that of bulk. From these HRXRD measurements, the BFO in-plane contraction strain was

$$\epsilon_{\parallel} = -0.0053,$$

and the out-of-plane

extension strain was $\epsilon_{\perp} = 0.021$. Using these measured strain values, the experimental Poisson's ratio for BFO was computed as 0.25, which is in the expected range for metal oxides. The value itself indicates that for every time the in-plane biaxial strain increases by 1, the out-of-plane strain will respond by a factor of 4 increase.

The mosaic structure of the BFO film was also investigated by performing rocking curve scans about the BFO (001) Bragg peak. As shown in Figure 11, the FWHM of the rocking curve scan is approximately 0.086° ; this width corresponds to the BFO mosaic and the 0.05° incident beam angular width added in quadrature. Though the BFO film is made up of single crystals with a preferred (001) orientation, it has an angular mosaic width of 0.07° . However, this mosaic is considered relatively small, which means the BFO thin film was highly organized into single crystals. From the STO rocking curve, it was determined that the STO substrate mosaic was less than the 0.05° instrument resolution.

Conclusion

X-ray characterization of a magnetoelectric multiferroic BFO thin film on an intermediate SRO layer grown atop an STO (001)-oriented substrate was performed. Information regarding the structural features of the BFO film and SRO layer was extracted through the use of high-angle x-ray diffraction and low-angle XRR. The SRO intermediate layer was found to be highly planar, as the domain size roughly equaled its thickness, indicating a coherently strained layer throughout its thickness of 330 Å. X-ray investigations of the BFO thin film illustrated single-crystal quality, which was demonstrated by a miniscule mosaic structure. Additionally, it was found that the BFO thin film experienced contraction strain in the in-plane direction and extension strain in the out-of-plane direction, as hypothesized. Thus, the 550 Å thick BFO film can be classified as a rather coherently strained single crystal. More detailed analysis needs to be conducted on the film to work out the structural details. Extensive interface analysis must be performed to determine the specific roughness values; in this experiment, it was concluded that the three interfaces had roughness values on the scale of 6 Å, but further investigation should be carried out to calculate the unique roughness of each specific interface. Future work should include a comparative analysis of BFO thin films grown with different thicknesses and by different techniques such as PLD, molecular beam epitaxy (MBE), and metal-organic chemical vapor deposition. Also, further study should be performed to investigate the effect of an intermediate layer, such as the conductive oxide SRO, on the single-crystal quality of a BFO thin film.

This research was supported primarily by the Nanoscale Science and Engineering Initiative of the National Science Foundation under NSF Award Number EEC-0647560. Any opinions, findings and conclusions or recommendations expressed in this material are those of the author(s) and do not necessarily reflect those of the National Science Foundation.

References

- (1) Ramesh, R.; Spaldin, N. A. *Nature Mater.* **2007**, *6*, 21–29.
- (2) Béa, H.; Bibes, M.; Fusil, S.; Bouzehouane, K.; Jacquet, E.; Rode, K.; Bencok, P.; Barthélémy, A. *Phys. Rev. B.* **2006**, *74*, 020101(R).
- (3) Eerenstein, W.; Mathur, N. D.; Scott, J. F. *Nature.* **2006**, *442*, 759–765.
- (4) Auciello, O.; Scott, J. F.; Ramesh, R. *Phys. Today.* **1998**, *51*, 22–27.
- (5) Wang, J.; Neaton, J. B.; Zheng, H.; Nagarajan, V.; Ogale, S. B.; Liu, B.; Viehland, D.; Vaithyanathan, V.; Schlom, D. G.; Waghmare, U. V.; Spaldin, N.A.; Rabe, K. M.; Wuttig, M.; Ramesh, R. *Science.* **2003**, *299*, 1719.
- (6) Wie, C. R. *Mater. Sci. Eng. R.* **1994**, *13*, 1–56.
- (7) Miceli, P. F. X-ray Reflectivity from Heteroepitaxial Layers. In: Feng, Z. C., ed. *Semiconductor Interfaces, Microstructures and Devices: Properties and Applications*. Institute of Physics: Bristol, **1993**: 87–114.
- (8) Jona, F.; Shirane, G. *Ferroelectric Crystals*. Dover: New York, **1993**: 216–261.
- (9) Kubel, F.; Schmid, H. *Acta. Cryst. B.* **1990**, *46*, 698–702.
- (10) Ederer, C.; Spaldin, N. A. *Phys. Rev. B.* **2005**, *71*, 224103.
- (11) Callister, W. D. *Materials Science and Engineering: An Introduction*. John Wiley & Sons: New York, **2000**: 30–59.
- (12) Cullity, B. D.; Stock, S. R. *Elements of X-ray Diffraction*. Prentice Hall: Upper Saddle River, NJ, **2001**: 1–28.
- (13) Hammond, C. *The Basics of Crystallography and Diffraction*. Oxford UP: New York, **2001**: 104–120.
- (14) Thompson, C.; Foster, C. M.; Eastman, J. A.; Stephenson, G. B. *Appl. Phys. Lett.* **1997**, *71*, 3516–3518.
- (15) Als-Nielsen, J.; McMorrow, D. *Elements of Modern X-Ray Physics*. John Wiley & Sons: New York, **2001**: 61–106.
- (16) Fewster, P. F. *X-ray Scattering from Semiconductors*. Imperial College: London, **2003**: 1–21.
- (17) Lautrup, B. *Physics of Continuous Matter*. Institute of Physics: Bristol, **2005**: 135–144.
- (18) Dunn, M. L.; Ledbetter, H. *J. Mater. Res.* **1995**, *10*, 2715–2722.
- (19) Srikant, V.; Speck, J. S.; Clarke, D. R. *J. Appl. Phys.* **1997**, *82*, 4286–4295.